Manuscript Number 7348R1

Revision 3

Formation pathway of norsethite dominated by solution chemistry under ambient conditions

Yi-Fan Zhang[1], Qi-Zhi Yao[2]*, Fei-Jin Qian[1], Han Li[1], Gen-Tao Zhou[1, 3]*, Sheng-Quan Fu[4]

[1] CAS Key Laboratory of Crust-Mantle Materials and Environments, School of Earth and Space Sciences, University of Science and Technology of China, Hefei 230026, P. R. China.

[2] School of Chemistry and Materials Science, University of Science and Technology of China, Hefei 230026, P. R. China.

[3] CAS Center for Excellence in Comparative Planetology, University of Science and Technology of China, Hefei 230026, P. R. China.

[4] Hefei National Laboratory for Physical Sciences at Microscale, University of Science and Technology of China, Hefei 230026, P. R. China.

Corresponding author: Prof. Dr. Gen-Tao Zhou

Tel.: +86 551 63600533

Fax: +86 551 63600533

Email: gtzhou@ustc.edu.cn

Dr. Qi-Zhi Yao

Tel.: +86 551 63601596

Email: qzyao@ustc.edu.cn

Abstract

Recently dolomite analogues including norsethite, kutnahorite and $PbMg(CO_3)_2$, etc. have attracted much attention due to their dolomite-like crystallographic structure and the resulting potential in solving "dolomite problem". Previous studies indicate that mechanisms that underlie the formation of norsethite exhibit some similarities to pathways of dolomite crystallization. However, the crystallization behavior of norsethite is still poorly understood, and the physicochemical factors regulating the process are not yet fully established. Herein, in order to determine the relationships between solution chemistry and formation pathway of norsethite, a series of experiments for the synthesis of norsethite from the solutions with different concentrations of Mg^{2+} and Ba^{2+} by a CO_2 gas-diffusion method were carried out under ambient conditions. The morphology and phase composition of the products were investigated by a range of techniques including XRD, FESEM, micro-Raman and FTIR techniques. ICP-AES was used to monitor the evolution of the concentrations of Mg^{2+} and Ba^{2+} in the mineralization solutions. Our observations suggest that formation pathway of norsethite strongly depends on Mg/Ba ratio in solution, and pure norsethite can directly crystallize from the solutions with Mg/Ba ratio ranging in 20-40. This is the first time to report the direct precipitation of dolomite analogues at ambient temperatures. It suggests that direct precipitation is a feasible pathway for cation ordering structure formation under ambient conditions.

Keyword: norsethite; dolomite analogue; formation pathway; dolomite

Introduction

The "dolomite problem" is a long-standing puzzle in geology (e.g., Warren, 2000; Gregg et al., 2015). A fundamental question involved in the low-temperature formation of mineral dolomite is its mineralization pathway and mechanism. Two main mechanisms, primary precipitation and dolomitization, have been proposed and widely discussed in past two centuries. It has been speculated that the switch between "direct" dolomite precipitation and indirect "dolomitization" as the formation pathway may be related to the changes in ocean chemistry over time (Hood et al., 2011; Rodriguez-Blanco et al., 2015). However, because of the kinetic difficulty in synthesizing dolomite in laboratory under ambient conditions (e.g., Land, 1998), the argument of dolomite formation pathways cannot be settled by laboratory experiments, and physicochemical conditions for controlling dolomite formation is still ambiguous (Gregg et al., 2015; Rodriguez-Blanco et al., 2015).

An investigation on the formation pathways of minerals with dolomite-like structure could be a feasible strategy to enhance our comprehension of dolomite formation. The dolomite characteristic structure with double cations ordered arrangement can be found in several carbonates, such as norsethite ($BaMg(CO_3)_2$) (Böttcher, 2000; Zheng and Böttcher, 2016), ankerite ($CaFe(CO_3)_2$) (e.g., Chai and Navrotsky, 1996), kutnohorite ($CaMn(CO_3)_2$) (e.g., Frondel and Bauer, 1955; Peacor et al., 1987), $PbMg(CO_3)_2$ (Morrow and Ricketts, 1986; Pimentel and Pina, 2016), $SrMg(CO_3)_2$ (Froese, 1967), $BaMn(CO_3)_2$ (Böttcher et al., 2012a; Böttcher et al., 2012b; Schmidt et al., 2013), $CdMg(CO_3)_2$ (Tareen et al., 1995; Bromiley et al., 2007) etc. Most of these carbonates have been reported from either natural observations or laboratory experiments. Only few have been both found in natural environments and obtained in laboratory, and norsethite is one of them. The crystal structure of norsethite belongs to a group of R-centered trigonal double carbonates. Two cations, barium and magnesium, are arranged in layers parallel to (001) with the triangular CO_3 groups interconnecting them. Thus, norsethite has been considered as one of dolomite-analogues based on its fundamental cation ordering structure. Superstructure diffractions (*h0l*) and (*0kl*) with *l* odd (e.g., (105), (021), (101) etc.), which are the specific

signature of dolomite cation ordering structure, can also be observed on X-ray diffraction pattern of standard norsethite (Mrose, 1961; Lippmann, 1968; Effenberger and Zemann, 1985; Böttcher et al., 1997; Ende et al., 2017).

The mineral norsethite was found in wide range of natural settings including sedimentary, hydrothermal and metamorphic environments (Mrose, 1961; Steyn and Watson, 1967; Böttcher et al., 1997) and in carbonatites (Platt and Woolley, 1990). In laboratory, norsethite was first synthesized at 500 °C (Chang, 1964), and its low-temperature precipitation was later achieved by several researchers (Lippmann, 1967, 1968; Hood et al., 1974; Morrow and Ricketts, 1986; Pimentel and Pina, 2014, 2016; Lindner and Jordan, 2018; Lindner et al., 2018). In most cases, norsethite were obtained by a reaction (Equation 1) analogous to dolomitization process, namely a conversion from solid witherite ($BaCO_3$) to norsethite through interaction with solutions containing magnesium chloride and sodium bicarbonate (Lippmann, 1968; Morrow and Ricketts, 1986; Lindner and Jordan, 2018). Besides, Mg-containing carbonates, such as nesquehonite, magnestite, or norsethite itself, were also used as starting materials or seed crystals in synthesis of norsethite (Böttcher, 2000; Lindner et al., 2017; Lindner et al., 2018). Several studies attempted to precipitate norsethite "directly" from aqueous solution containing two cations and CO_3^{2-}. However, it turned out that norsethite crystallizes from various precursors (e.g., amorphous phases, northupite, eitelite, witherite, etc.) but not strictly as Equation 2 (Hood et al., 1974; Pimentel and Pina, 2014, 2016). Although Lippmann (1973) has pointed out very early that norsethite does not form directly as a precipitate from solutions, Hood et al.(1974) stood for Eq. 2 based on the inverse relation between the concentrations of Ba^{2+} and Mg^{2+} in remaining solution, and the direct precipitation of norsethite under ambient conditions has not been achieved yet.

$$BaCO_3 + Mg^{2+} + CO_3^{2-} = BaMg(CO_3)_2 \quad \text{..... (1)}$$

$$Ba^{2+} + Mg^{2+} + 2CO_3^{2-} = BaMg(CO_3)_2 \quad \text{..... (2)}$$

In this paper, we present a series of experiments to synthesize norsethite under ambient conditions by a CO_2 diffusion method. The results suggest that the formation of norsethite strongly depends on the Mg/Ba ratio in solutions and its formation pathway varies in different parenting solutions. Furthermore, the direct precipitation of norsethite can be successfully

achieved at Mg/Ba ratio ≥ 20 and adequate CO_3^{2-} conditions. To the best of our knowledge, it is the first time to crystallize dolomite analogues through direct precipitation at ambient temperature. The findings reported in this paper provide new insights into formation pathways of dolomite analogues and even dolomite.

Experimental procedures

Chemicals

All starting chemicals are commercially available and used as received without further purification. Analytical grade ('*pro analysi*') ammonium carbonate ($(NH_4)_2CO_3$), barium chloride dihydrate ($BaCl_2 \cdot 2H_2O$), magnesium chloride hexahydrate ($MgCl_2 \cdot 6H_2O$), and hydrochloric acid (HCl) were purchased from Sinopharm Chemical Reagent Co., Ltd. Deionized water (pH = 5.74) was used for the experiments. All glassware including glass beakers and substrates are cleaned and sonicated in ethanol for 5 min, rinsed with distilled water, and finally dried at 80 °C.

Mineralization

The mineralization of norsethite was carried out by a CO_2 gas diffusion technique as described by Zhou et al. (2010). All experiments were run at room temperatures (25 ± 1 °C) for durations ranging from 30 min to 48 h. The starting solutions were prepared from $BaCl_2 \cdot 2H_2O$ and $MgCl_2 \cdot 6H_2O$ in different proportions using deionized water, and the detailed experimental parameters are listed in Table 1. In a typical procedure, 50 mL of Ba^{2+}-Mg^{2+} solution was transferred into a 50-mL beaker with a clean square glass microscopy cover slip (18×18 mm) on the bottom to collect solid precipitate. Then the beaker was covered with Parafilm with eighteen punched needle holes and placed into a closed desiccator. A small beaker with 25 g of ground ammonium carbonate was placed in the middle of the desiccator as the source of CO_2, while a petri dish containing 100 mL H_2SO_4 (98 wt%) was put on the bottom of the desiccator to scavenge NH_3 vapor. After a given mineralization duration (Tables 1 and 3), the beaker was moved out of the desiccator and the mineralization was

terminated by denying access to CO_2. The glass cover slip was removed from the solution, alternately rinsed carefully with distilled water and anhydrous ethanol three times, and allowed to dry in a vacuum oven at room temperature. The initial and final pHs of the mineralization solution were measured by a pH-meter (Inolab WTW series pH 740). Moreover, the finally mineralized solution was filtered with a 0.22 μm pore size membrane filter to remove possibly suspended particles, and then an aliquot of the mineralized solution was immediately acidified with 1 M HCl solution for determination of dissolve cation concentrations. Meanwhile, the concentrations of CO_3^{2-} and HCO_3^- ($[CO_3^{2-}]$ and $[HCO_3^-]$) were determined by acid base titrations with double indicators (0.5% m/v phenolphthalein and 0.1% m/v methyl orange). Considering that NH_3 in solution is an important confounder in titration, another method depending on the total concentration of inorganic carbon (TIC) and ionization equilibrium was also used to determine the concentration of CO_3^{2-} and HCO_3^-. The TIC was measured by adding excess $BaCl_2$ solution into another aliquot of the supernatant and weighing the precipitated witherite ($BaCO_3$). Then the concentration of CO_3^{2-} could be calculated by ionization equilibrium (3) and (4):

$$H_2CO_3 = H^+ + HCO_3^- \qquad Ka_1 = 4.2\times10^{-7} \qquad \text{..... (3)}$$

$$HCO_3^- = H^+ + CO_3^{2-} \qquad Ka_2 = 5.6\times10^{-11} \qquad \text{..... (4)}$$

Assuming activities equal to concentrations, the minimum carbonate concentration required for oversaturation with respect to specific mineral witherite and norsethite at initial Mg/Ba ratios, as listed in Table 1, was calculated using the following expressions:

$$[Ba^{2+}][CO_3^{2-}] = K_{sp,wit} \qquad \text{for witherite } (BaCO_3)$$

$$[Ba^{2+}][Mg^{2+}][CO_3^{2-}]^2 = K_{sp,nor} \qquad \text{for norsethite } (BaMg(CO_3)_2)$$

The solubility products of witherite, $K_{sp,wit}=10^{-8.56}$ and the solubility products of norsethite, $K_{sp,nor} = 10^{-17.73}$ are taken from the PHREEQC.DAT database and Lindner et al. (2018), respectively. In addition, Visual MINTEQ was used to compute the saturation state of solutions with respect to relevant mineral phases, and the database was modified by inserting the solubility products of norsethite.

Characterization of product materials

To study crystal morphology, the 18×18 mm glass cover slips with mineralized products were sputter-coated with gold in a SPI-MODULE device (90 s, 24 mA) (or with platinum in a Bal-Tec SCD 050 sputter coater at plasma current 36 mA for 90 s) to reduce charging effects upon e-beam exposure, and then fixed into an aluminum stand with electrically-conducting tape. Scanning electron microscopy (SEM) analysis was done in a field emission SEM instrument (JEOL JSM-6700F) with energy-dispersive X-ray spectrometer (EDX) for element analysis (Oxford Xmax). The SEM instrument was operated at high vacuum (~10^{-5} Pa), acceleration voltage 3 kV, emission current 10 μA. EDX spectra were acquired for 30s with nominal spot diameter 1 μm, at acceleration voltage 15 kV and working distance 14 mm, keeping detector dead time <30%.

After assessment by SEM-EDX, Raman spectra were collected by inserting the glass slides in a Jobin-Yvon Horiba LabRam HR Evolution micro-Raman probe using 532 nm Ar laser excitation. The beam diameter for the Raman spectroscope is ~1 μm. Monocrystalline silicon Si was used for internal calibration of the Raman spectra.

Moreover, X-ray powder diffraction (XRPD) patterns were recorded on a Rigaku Smartlab 9 kW (Japan) X-ray diffractometer with Bragg-Brentano geometry, using Ni-filtered Cu Kα irradiation (λ = 0.154184 nm), with a goniometer radius of 300 mm. The Soller collimator on the primary beam exhibited a divergence of 5.0°, whereas the incident slit (IS) and two receiving slit (RS1 and RS2) were set at 1/2°, 20 mm and 20 mm, respectively. Diffractograms were recorded from 10 to 70° 2θ in 0.01° 2θ increment and with a scanning rate of 10°/min. For samples collected at an early stage of mineralization, the glass slide bearing a limited amount of precipitate was directly placed in a dimpled glass sample holder; for the products with sufficient quantity, the precipitates were scraped from the glass slides, dry-ground by using an agate mortar for ~1 min, and then mounted on a monocrystalline silicon substrate known as a zero-background plate. Next, the samples were introduced into the diffractometer instrument, and specimen height was adjusted following standard procedures. Peaks were indexed according to the ICDD PDF-2 database for phase identification.

Finally, the FT-IR spectra were recorded at room temperature on a PerkinElmer Frontier FT-IR spectrometer by the method of KBr pellets. To increase reflectance and avoid spectral

distortion and nonlinearities, ~1 mg of precipitate was scraped from the glass slides, mixed with ~150 mg KBr (FT-IR grade), finely ground, and compressed to a 200–250 μm thick pellet in a KEQI 769YP-30T hydraulic press device at 20 MPa for 60 s. The spectral resolution was 1 cm^{-1} and the scanning range was from 400 to 4000 cm^{-1}. All spectra were baseline corrected, and compared with Chukanov (2014) and Böttcher et al. (1997) for reference.

In addition to the characterization of the precipitated solids, the acidified supernatant solutions above were diluted with deionized water into appropriate concentration range (cation concentration: 1-100 mg/L) to ensure the accuracy and precision of measurement. The diluted solution was analyzed by inductively-coupled plasma atomic emission spectroscopy (ICP-AES) in a Perkin-Elmer Optima 7300DV instrument to determine Ba and Mg concentrations. For each experiment, three replicate supernatant samples were prepared and analyzed.

Results

Characterization of mineralized products

The mineralization experiments were first conducted at different Mg/Ba ratios (Table 1). After 40 min of mineralization, a series of FESEM analyses reveal that no visible precipitate can be found on the glass slides at Mg/Ba = 50/10 or 50/5, but a few spindle-like particles scattered on the glass slides at Mg/Ba = 50/25 (e.g., Fig. 1, panel a1), indicating that higher concentration of Ba^{2+} facilitates the carbonatization. EDX analyses reveal that the spindle-like particles contain elements Ba, C and O (the Au sign from the sample preparation for FESEM analysis) (Fig. S1). Considering the limited amount of the precipitates, micro-Raman spectroscopy technique was adopted to further identify the particles. The vibrational bands around 1059, 690, 225 and 136/150 cm^{-1} can be well assigned to the internal stretching (ν_1) and bending (ν_4) vibrations of the C-O bonds in the carbonate groups, and the external translational (T) and librational (rotatory) (L) modes of witherite, respectively (Buzgar and Apopei, 2009; Wang et al., 2019), demonstrating that the spindle-like particles are witherite (Fig. 1, inset in panel a1). With the mineralization prolonging to 1 h, the spindle-like crystals

226 further grow into branched rod-like structures at their two ends (e.g., Fig. 1, panel a2).
227 Meanwhile, a few spherulitic aggregates with an "eye" structure can be observed by FESEM
228 on the glass substrates at Mg/Ba = 50/10 or 50/5 (Fig. 1, panels b1 and c1). The EDX (data
229 not shown) and micro-Raman analyses also confirm that they are all pure witherite (e.g.,
230 panel b2 in Fig. 1 and Fig. S2a). At the mineralization time of 2 h, the branched rod-like
231 witherite crystals have developed into the dumbbell-shaped or spherical clusters with a
232 diameter of ~10 μm (Fig. 1, panel a3), while larger spherical clusters with a diameter of 40-50
233 μm occur at Mg/Ba = 50/10 (Fig. 1, panel b3). The magnified FESEM images reveal that
234 these cluster-like structures are all constructed by nano-rods (Fig. 1, insets in panels a3 and
235 b3). For the precipitates harvested at the Mg/Ba = 50/5, however, the FESEM analyses
236 unambiguously reveal two different kinds of morphological features (e.g., Fig. 1, panel c2),
237 i.e., the large spherulitic structures aggregated by nano-rods and the small aggregates
238 consisting of rhombohedra with a mean size of 5 μm (Fig. 1, panels c3 and c4). The EDX
239 analyses show that the large spherulites contain elements Ba, C and O (Fig. 1, panel c3),
240 while the small ones add extra element Mg, and their Mg/Ba are close to 1:1 (Fig. 1, panel c4).
241 Further powder XRD analyses were performed on the samples after 2 h of mineralization, and
242 the typical XRD patterns are depicted in Fig. 2. Compared with the standard patterns of
243 witherite and norsethite, the precipitates obtained at Mg/Ba of 50/25 and 50/10 are all
244 phase-pure witherite with space group P*mcn* (62) and lattice constants a = 5.280 Å, b = 8.830
245 Å and c = 6.390 Å (JCPDS file 44-1487). However, for Mg/Ba = 50/5, as can be seen from
246 Fig. 2c, the peaks at 29.6, 23.0 and 21.1^{o} 2θ, which can be indexed as (104), (012) and the
247 superstructure diffraction (101) of norsethite, can be clearly discerned on the XRD pattern (as
248 highlighted by red asterisks), indicating that besides witherite, norsethite with cation ordering
249 structure has formed after 2 h of mineralization. Combining with the FESEM, EDX and
250 Raman results (Fig. 1, panels c2-4, and Fig. S2b-d), it can easily assign the large spherical
251 aggregates as witherite, but the small rhombohedral ones as norsethite, and the rhombohedral
252 feature is also consistent with the growth habit of norsethite with R-center trigonal group. It
253 should be noted that there is no spatial association between crystallization sites of the two
254 kinds of aggregates, indicating that norsethite crystals may directly crystallize from the
255 solution, but not from transformation of witherite to norsethite.

Nevertheless, with the mineralization proceeding, norsethite can also be detected in the products at Mg/Ba of 50/25 and 50/10 (Fig. 3), and the time for the first detection of norsethite (t_{nor}) is 12 and 6 h, respectively. The FESEM analyses of the products at t_{nor} (Fig. 4a and b) show that a small number of well-developed rhombohedra with a mean size of 5 μm, which can be assigned as norsethite, coexist with witherite rod-like clusters. These neo-norsethite crystals locate separately with preexisting witherite aggregates, similar to the observation on panel c2 in Fig. 1, indicating that they should also directly crystallize from the solution. In particular, besides the rhombohedra aggregates isolated from the witherite spherulites, a few rhombohedral crystallites attaching to the witherite spherulites can be found in the product at Mg/Ba = 50/10 (Fig. 4b and its inset). The EDX analyses reveal that these rhombohedra consist of the elements Ba, Mg, C and O, and the Mg/Ba is close to 1:1, demonstrating that they are norsethite as well (e.g., Inset in Fig. 4b). These attached norsethite crystals may be produced via a transformation from precursor witherite to norsethite. Furthermore, as mineralization time prolongs to 12, 24 and 48 h, a series of FESEM observations unveil that an increasing quantity of rhombohedra present on the witherite spherulites, and these obtuse rhombohedral crystals gradually grow into larger, perfect rhombohedra (~10 μm) (e.g., Fig 4c and d) concomitantly with rod-like witherite crystals dissolving into smaller particles (~200 nm) (e.g., Fig. 4d and its inset), finally develop into spherical aggregates (e.g., Fig. 4e), inheriting the size and shape of spherulitic witherite precursor. Similar phenomena were also observed in the experiments with Mg/Ba of 50/25 and 50/5 (Fig. S3). These results indicate that a multi-step pathway, including individual precipitation of witherite and norsethite, and subsequent transformation from witherite to norsethite, occurs during the mineralization.

Figure 5 plots percent norsethite vs. time at the three different Mg/Ba ratios, as calculated from the diffractograms by using semi-quantitative RIR method (Hubbard and Snyder, 1988). It can be seen from Fig. 5 that the length of the induction period of norsethite is negatively correlated with the initial Mg/Ba ratio. Meanwhile, the proportion of norsethite progressively increases with mineralization proceeding in each experiment, indicating that the continuous precipitation of norsethite and dissolution of witherite concomitantly occur after t_{nor}, in consistent with the FESEM observations (e.g., Fig. 4c-e). Moreover, the weight% of

norsethite in all the experiments displays an unambiguous positive correlation with initial Mg/Ba ratio, and 95.0, 67.0 and 63.7 wt% of norsethite are achieved at 48 h, respectively, indicating that the difference in mineralizing solution chemistry may significantly affect the carbonatization kinetics, leading to the formation of various Ba/Mg carbonates. Considering the difference in mineralization induction time at each experiment, it further suggests that solution chemistry in the mineralization system synchronously exert a crucial control over the formation of norsethite.

Solution chemistry of the mineralization system

To further understand the solution chemistry-dependent mineralization of norsethite, the concentrations of CO_3^{2-}, Mg^{2+}, Ba^{2+} in solution ($[CO_3^{2-}]$, $[Mg^{2+}]$, $[Ba^{2+}]$) as well as pH at different mineralization times were systematically monitored. Here, two different methods, as described in Section 2.2, were used to measure $[CO_3^{2-}]$, and the results are listed in Table S1. Compared with the minimum $[CO_3^{2-}]$s for oversaturation of witherite and norsethite (Table 1), the $[CO_3^{2-}]$ in mineralization solutions are over three orders of magnitude higher in all the experiments regardless of the measuring methods. Therefore, it can be tentatively considered that the mineralizing solutions are oversaturated either for witherite or norsethite.

Figure 6 illustrates the time-dependent evolutions of pH, $[Mg^{2+}]$ and $[Ba^{2+}]$ at the different initial Mg/Ba ratios. The pHs at the three Mg/Ba ratios all rapidly increase to ca. 8.5, and slightly fluctuate between 8.5~9.0 during subsequent mineralization. However, the consumptions of Ba^{2+} and Mg^{2+} in solution are asynchronous in each experiment. The $[Ba^{2+}]$ declines much faster than $[Mg^{2+}]$ prior to t_{nor}, and approaches to zero at 12 h, indicating that witherite forms first and Ba^{2+} in solution is completely precipitated after 12 h. In contrast, the $[Mg^{2+}]$ falls faster after t_{nor}, indicating that the much more consumed Mg^{2+} ions are sequestered into growing norsethite crystals. Especially after 12 h of mineralization, $[Mg^{2+}]$ continuously declines while $[Ba^{2+}]$ almost remains unchanged, indicating the dissolution of precursor witherite and concurrent precipitation of norsethite. Therefore, the different evolutions of $[Mg^{2+}]$ and $[Ba^{2+}]$ reveal that a multi-step pathway including the pre-precipitation of witherite prior to t_{nor}, and the subsequent formation of norsethite around t_{nor}, as well as the transformation from witherite to norsethite occurs, being consistent with

316 XRD and FESEM analyses (Figs. 1-4). Here, the special attention is paid on the solution
317 chemical parameters at t_{nor}. Interestingly, there is a remarkable similarity in solution
318 chemistry at t_{nor} (Table 2). Specifically, the pHs are around 8.5-8.8 at all the Mg/Ba ratios.
319 The $[Mg^{2+}]$s are 45.23, 47.59, 49.10 mM, and the $[Ba^{2+}]$s 2.17, 1.30, 1.88 mM, respectively. It
320 corresponds to a Mg/Ba ratio of 20.84, 36.61 and 26.12, which are much higher than the
321 initial Mg/Ba ratio of 2, 5 and 10. These results indicate that the nucleation and growth of
322 norsethite occur in alkaline solution with high $[Mg^{2+}]/[Ba^{2+}]$ ratio.
323
324 **Direct precipitation of norsethite**
325 To further confirm the direct crystallization of norsethite from the solution, the initial
326 concentrations of Mg^{2+} and Ba^{2+} in mineralizing experiments were first adjusted to 50.0 mM
327 and 2.0 mM, corresponding to a Mg/Ba ratio of 25, which is close to the solution composition
328 at t_{nor} (Table 2), and the detailed experimental parameters are listed in Table 3. Here, the early
329 stages of the mineralization were carefully examined by a series of FESEM, micro-Raman
330 and XRD analyses. Before mineralizing for 1.5 h, the FESEM and micro-Raman observations
331 reveal that there is no visible change on the glass slides for collecting precipitates compared
332 with their original counterparts (e.g., Fig. S4a-d). The Raman analyses for the
333 randomly-selected spots on the glass slides show that except for the characteristic bands
334 belonging to sodium silicate glass, no precipitate of Ba/Mg carbonates can be detected (e.g.,
335 Fig. S4g). After 2 h of mineralization, however, FESEM analyses find sporadic particles with
336 an mean size of 500 nm on the glass slides (Fig. 7a). The larger particles (~3 μm in diameter)
337 can be observed at 3 h (Fig. 7b), indicating that the successive growth occurs. The EDX
338 analyses reveal that these particles contain elements Ba, Mg, C and O (the Si, Na and K signs
339 from the glass substrate) (e.g., inset in Fig. 7a). Corresponding micro-Raman analyses further
340 identify the particles as norsethite (Fig. 7c), i.e., the appearance of the vibrational bands at
341 1118, 700, 117 and 261 cm^{-1} assigned to the internal stretching (ν_1) and bending (ν_4)
342 vibrations of the C-O bonds in the carbonate groups, and the external translational (T) and
343 librational (rotatory) (L) modes of norsethite (e.g., Böttcher et al., 1997). The XRD analyses
344 for the glass slides with precipitate particles also show appearance of the characteristic (104),
345 (003) and (101) diffractions of norsethite, demonstrating that the earliest products are cation

ordered norsethite (e.g., Fig.S4h). These results indicate that norsethite can directly nucleate and grow from the solution. After 4 h of mineralization, more products formed, and thus powder XRD and FT-IR analyses were performed. Fig. 7d depicts the typical powder XRD pattern of the products, which can be exclusively indexed as norsethite with cation ordering structure. The FT-IR result (Fig. 7e) shows the characteristic vibrational bands of norsethite at 1120 (ν1), 879 (ν_2), 1461 (ν_3), 702 (ν_4), 1813 ($\nu_1 + \nu_3$) and 2552 ($\nu_1 + \nu_4$) cm^{-1} (Böttcher et al., 1997; Chukanov, 2014), but none of the characteristic vibrational bands of witherite at 1058, 857, 1751 and 2452 cm^{-1}, further indicating that the mineralized products contain no witherite. The panoramic FESEM image (Fig. 7f) show that the product uniformly consists of quasi-hexagonal particles with 5-7 μm in diameter. The enlarged image (Inset in Fig.7f) unveils that the quasi-hexagonal particles are the penetration twins of norsethite with well-developed {10.4} faces and apparent growth striations. As mineralization time further prolonging, the penetration twins grow into oblate spheroids with distinct rhombohedral features, and the size of crystals continuously increases (Fig. 7g-i and insets). XRD and FTIR analyses identified that they are norsethite as well, indicating that norsethite crystals persistently grow with CO_2 diffusing into the mineralization solution. Figure 8 depicts the profile of [Ba^{2+}], [Mg^{2+}], and pH vs. mineralization time. The pHs increase to ca. 8.5 at 1 h and fluctuate between 8.5~9.0 in the following mineralization. Remarkably, [Ba^{2+}] and [Mg^{2+}] in the mineralization solutions, as illustrated in Fig. 8, almost synchronously decrease, further confirming that the direct precipitation of stoichiometric norsethite without precursor phases occurs under current conditions.

Moreover, a series of experiments with a Mg/Ba ratio of 25 but varying cation concentrations (e.g., Table 3) were also performed. The micro-Raman analyses identify that the earliest visible precipitates are norsethite (e.g., Fig. S5). The powder XRD patterns reveal that the precipitates collected after 4 h of mineralization are all composed of single phase of cation ordered norsethite (Fig. S6). Note that even if the initial [Ba^{2+}] is as high as 16.0 mM, none of witherite and other precursors is detected in the mineralized product. It appears that high Mg/Ba ratio, rather than low [Ba^{2+}], is the prerequisite for direct nucleation of norsethite. In particular, the synchronous decrease of [Ba^{2+}] and [Mg^{2+}] in solution also supports the direct precipitation of norsethite from the solution (Fig. S7). Figure 9 presents FESEM images

of the precipitates. It can be found that the products are monodisperse and uniform crystals with a mean size of 5 μm, and there is an increasing yield with the increasing cationic concentrations. However, the magnified images (Insets in Fig. 9a-c) further reveal the different morphological features of the products, i.e., the crystals obtained at Mg/Ba of 25/1 consist of penetration twins and rhombohedra with well-developed {10.4} faces (Fig. 9a and its inset); the norsethite crystals from Mg/Ba of 100/4 and 200/8 are rhombohedra with obtuse edge showing a trend to form elongated crystals (e.g., Fig. 9b and its inset); while at Mg/Ba of 400/16, the crystals exhibit rugged surface and seem to be composed of submicrometre-sized rhombohedral subunits (Fig. 9c and its inset). These disparities in morphology and texture could result from different crystal growth rates, indicating that the growth kinetics of direct-crystallized norsethite vary at different cationic concentrations.

Furthermore, the mineralization experiments were also conducted at initial [Mg^{2+}] ranging from 80.0 to 2.0 mM when holding [Ba^{2+}] constant at 2.0 mM, corresponding to a Mg/Ba ratio from 40 to 1 (Table 3). According to XRD analyses (Fig. 10), except at Mg/Ba of 2/2, norsethite can be detected in the products after 4 h of mineralization. However, only at Mg/Ba of 40/2 and 80/2 is norsethite obtained as the exclusive phase, while the products at Mg/Ba $\leq$ 15 are the mixture of witherite and norsethite. These results reiterate the domination of Mg/Ba ratios on norsethite formation, and demonstrate that norsethite can be directly crystallized from the solutions with Mg/Ba in the range of 20-40. A close examination of primary norsethite morphologies at Mg/Ba of 10/2 to 80/2 reveals that norsethite obtained at different Mg concentrations are mostly rhombohedra with the great expression of the {10.4} faces (Fig. 11a-c), while at Mg/Ba of 80/2 the crystals are rhombohedra with obtuse edge (Fig. 11d), indicating that the high concentration of Mg^{2+} affects the growth of norsethite.

Discussion

The synthetic routes towards norsethite in previous studies can be categorized into two groups based on the species of starting materials: 1) reactions starting with simple solid carbonates, including norsethitization of solid $BaCO_3$ in contact with a Mg-rich solution

(Lippmann, 1968; Morrow and Ricketts, 1986; Lindner and Jordan, 2018), the reaction between magnesite and Ba-containing solution (Lindner et al., 2017), immersing witherite and nesquehonite into solutions of $NaHCO_3$ (Böttcher et al., 1997; Böttcher, 2000), dry grinding of the reactants $BaCO_3$ and $MgCO_3$ (Longo and Voight, 1989), and overgrowth experiments on norsethite seed crystals (Lindner et al., 2018), etc.; 2) reactions by mixing Ba-Mg solutions and Na_2CO_3 solution, in which norsethite forms by sequences of dissolution-crystallization processes involving an amorphous precursor and several crystalline precursors (eitelite, nesquehonite and northupite, etc.) (Hood et al., 1974; Pimentel and Pina, 2014, 2016). It appears that regardless of the methods used, the existence of solid precursor phases cannot be precluded in the formation of norsethite. Although Lindner et al. (2018) have suggested that all of these reactions, in principle, can be simplified to the net reaction as Equation 2, the direct crystallization of norsethite from aqueous solution has not been achieved yet. In our experiments, however, norsethite can be obtained without passing through any amorphous or crystalline precursor at initial Mg/Ba ratio higher than 20 under ambient conditions (e.g., Figs. S4, 7, 10, S5 and S6), and the synchronous decline of $[Ba^{2+}]$ and $[Mg^{2+}]$ in solution further confirm the direct crystallization of norsethite from the solution (e.g., Figs. 8 and S7). A series of FESEM analyses (e.g., Figs. 7f-i, 9, 11c and d) reveal that these directly precipitated norsethite crystals are highly crystalline rhombohedra or their aggregates including the penetration twins. The results provide direct observations of primary norsethite crystals originated from aqueous solution. In contrast, at lower Mg/Ba ratios ($\leq$ 15), witherite was always formed as the first product, followed by a mixture of witherite and norsethite (e.g., Figs. 1, 2, 10, S1 and S2), indicating that initial Mg/Ba ratio in solution exerts a dominant role in determining the Mg-Ba carbonatization pathways. In these cases, however, the initial precipitation of witherite necessarily leads to the gradual rise in Mg/Ba ratio (Fig. 6). As a result, the Mg/Ba ratios at t_{nor} have reached 20-37, much higher than their initial values (Table 2). Furthermore, the FESEM observations (Figs. 1c2, 4a and b, 11a and b) also distinctly reveal that the first-detected norsethite crystals at t_{nor} are spatially independent of the coexisting witherite, indicating that they directly grow up from mineralizing solution instead of transform from witherite. It again demonstrates that the high Mg/Ba ratio is indispensable for the nucleation of norsethite.

In fact, by revisiting the previous synthesis experiments of norsethite (e.g., Lippmann, 1968; Morrow and Ricketts, 1986), the formation of norsethite dependent on Mg/Ba ratio can be more clarified. In the classical norsethitization experiments, the only Ba^{2+} source is dissolving witherite, which apparently creates a solution chemical environment with high Mg/Ba ratios. According to Lippmann (1973)'s estimation, the ratio Mg/Ba in solutions can reach up to approximately 200 or 3000 in his norsethitziation experiments. Moreover, in the growth experiments on witherite seeds at 50 °C, witherite was the only product at Mg/Ba ratios ≤ 6, whereas norsethite precipitation occurred at Mg/Ba ≥ 12 accompanying with the dissolution of witherite (Lindner and Jordan, 2018). Similarly, Lindner et al. (2017) reported the crystallization of norsethite in the presence of magnesite seeds at 100 °C. In their experiments, it was the extremely low Ba^{2+} supply (≤ 0.14 mM) restricting norsethite growth, and the Mg/Ba ratios resulting in norsethite were fairly high. Even using solid witherite and nesquehonite ($MgCO_3 \cdot 3H_2O$) as the source of Ba^{2+} and Mg^{2+}, nesquehonite would initially dissolved completely and the following precipitation of norsethite was substantially the norsethitization reaction, which was characterized by high Mg/Ba ratio (Böttcher, 2000). These results demonstrate that ordered norsethite can precipitate out of the solutions with high Mg/Ba ratios, supporting the findings presented herein. However, the scenario is different in the cases of mixing Ba-Mg solution with Na_2CO_3 solution to form norsethite (Hood et al., 1974; Pimentel and Pina, 2014, 2016). In particular, Pimentel and Pina (2016) revealed that the crystallization of norsethite was inhibited at relatively high Mg/Ba ratio, which is in contrast to our observations that high Mg/Ba ratio facilitates norsethite formation. Note that the formation of an amorphous precursor prior to norsethite is an inevitable stage in their study, the inhibition should be attributed to the stabilizing role of Mg on the amorphous phase, as in the case of amorphous calcium carbonate (ACC) (e.g., Loste et al., 2003; Politi et al., 2010; Rodriguez-Blanco et al., 2012; Wang et al., 2015; Albéric et al., 2018). However, in present study using the CO_2 gas-diffusion method, the gradual diffusion of CO_2 into the Mg^{2+}-Ba^{2+} solution leads to a relative low carbonate concentration, thus avoiding an instantaneous high supersaturation and the formation of amorphous phases. Therefore, the inhibition effect does not occur.

As an anhydrous Mg-containing carbonate, the formation of norsethite is likely to be controlled by Mg^{2+} dehydration (Lindner et al., 2018), similar to the case of dolomite and magnesite (e.g., Deelman, 2003; Xu et al., 2013). Lippmann (1973) proposed that the likelihood of Mg^{2+} ions being absorbed at a cation site on a growing crystal is much smaller than for Ba^{2+} ions since the tight hydration results in very few Mg^{2+} breaking their hydration envelope and being sufficiently activated. Morrow and Ricketts (1986) also pointed out that there may be a threshold value of the Mg concentration in solution for "norsethitization" to occur, and this threshold concentration is not a simply mass balance requirement. In such scenario, high Mg/Ba ratio in solution increases the possibility for activated Mg^{2+} filled into Mg^{2+} sites in the structure of norsethite, favoring norsethite formation. Actually, the facilitation of high Mg/Ba ratio on norsethite formation somewhat coincides with previous observations on the influence of Mg/Ca on the formation of Mg-containing Ca-carbonates (e.g., Loste et al., 2003; Segev and Erez, 2006; Ries, 2009; Wang et al., 2009; Kaczmarek and Sibley, 2011). For example, numerous studies involving Mg-containing calcite showed that there is a positive correlation between the Mg/Ca ratio in fluids and Mg/Ca in abiotic and biotic calcite (e.g., Ohde and Kitano, 1978; Given and Wilkinson, 1985; Segev and Erez, 2006; Ries et al., 2008; De Choudens-Sanchez and Gonzalez, 2009; Ries, 2009; Hasiuk and Lohmann, 2010). Without organic additives, the Mg content in ACC is also dependent on the Mg/Ca ratio in solution (e.g., Loste et al., 2003; Wang et al., 2009; Wang et al., 2015). Moreover, high-temperature dolomitization experiments demonstrated that the solutions with higher Mg/Ca yield more stoichiometric dolomite (but not completely ordered) (e.g., Gaines, 1974; Sibley, 1990; Sibley et al., 1994; Kaczmarek and Sibley, 2011). Admittedly, the influence of Mg/Ca in solution on Ca-Mg-CO_3 system is more complex involving the variation in polymorph mineralogy and crystallization mechanism. These results indicate that high proportion of Mg^{2+} in solution facilitate more Mg^{2+} ions into solid carbonate phase, supporting the conclusion in present study.

However, note that both Mg-calcite and ACC are not cation-ordering, and it is still difficult to precipitate ideal dolomite even at high Mg/Ca ratios, indicating that the cation ordering is also crucial in the formation of dolomite analogues. As is known, the large discrepancy between Ba and Mg coordination schemes in norsethite structure energetically

favors the occurrence of ordered norsethite under ambient conditions (Pimentel and Pina, 2016; Lindner and Jordan, 2018). Simultaneously, given the ready precipitation of fully-ordered norsethite in our experiments and previous literatures (e.g., Lippmann, 1968; Hood et al., 1974; Böttcher, 2000; Pimentel and Pina, 2014, 2016; Lindner et al., 2017; Lindner and Jordan, 2018; Lindner et al., 2018), it follows that Mg^{2+} dehydration rather than cation ordering is the rate-limiting step during the formation of norsethite. Therefore, high Mg/Ba ratio in solution permits more activated Mg^{2+} to incorporate into the growing crystals, facilitating the nucleation of ordered norsethite. Additionally, Lindner et al. (2018) proposed that a given norsethite surface can promote the dehydration of Mg^{2+} by its certain structural surface configuration weakening the stability of adsorbed hydrous Mg-complexes. This mechanism could also play a role in the growth of norsethite in current study.

In present study, a variety of norsethite morphologies ranging from well-developed rhombohedra to rhombohedra with obtuse edges, penetration twins, oblate spheroids and spherical aggregates (Figs. 4, 7f-i, 9, 11 and S3), were obtained at different concentrations of Ba^{2+} and Mg^{2+}. Especially the norsethite transformed from precursor witherite tends to inherit the outline of the precursor to a great extent, i.e., forming the spherulitic aggregates consisting of rhombohedral subunits (Figs. 4 and S3). In contrast, the primary norsethite are generally rhombohedra or penetration twins with well-defined {10.4} faces (e.g., Figs. 1c2, 4a and b, 7e, 9 and 11). In previous growth experiments, the norsethite formed usually as columnar or prismatic crystals (Lindner and Jordan, 2018; Lindner et al., 2018; Lindner et al., 2017; Lippmann, 1968; Lippmann, 1973). Pimentel and Pina (2014, 2016) has reported the formation of norsethite spherulites aggregated by rhombohedral subunits during the aging of an amorphous precursor. It appears that the growth habit of norsethite varies with different formation pathways, and the secondary norsethite undergoing precursor transformation potentially often possesses the morphological feature of the precursors.

Implications

This experimental study provides a new insight into the formation pathways of norsethite

under ambient conditions. Our results indicate that the direct precipitation of norsethite is kinetically controlled by solution chemistry, i.e., high Mg/Ba ratios (>20), basic pH (~8.5), and sufficient CO_3^{2-}. In contrast, at lower Mg/Ba ratios (<15), a multi-step mineralization process is always involved, i.e., a precursor witherite first forms, followed by norsethite precipitation and transformation from precursor witherite to norsethite. To the best of our knowledge, this is the first report on direct crystallization of norsethite from aqueous solution under ambient conditions. It provides the new possibilities for further investigating growth kinetics, cation-ordering process and Mg dehydration in norsethite formation. Moreover, the mineralization pathway-dependent variation in morphology of norsethite, especially the inheritance of precursors' morphology and structure, can provide an opportunity to distinguish natural norsethite with different origins, and thus give a deep insight into the local environments where norsethite mineralization occurred.

Our findings also have important implications for better understanding the influence of local solution chemistry on dolomite formation. Geological observations revealed that modern dolomite forms as primary precipitates in a restricted number of hypersaline environments, i.e., evaporitic lakes or sabkhas (e.g., Miser, 1987, Warren, 2000, Lindtke et al., 2011), and Folk and Land (1975) pointed out that high Mg/Ca ratio is necessary for dolomite crystallization in these hypersaline environments. Hood et al. (2011) and Hood and Wallace (2012) suggested that the environmental conditions that dominate and promote the "direct precipitation" of dolomite from solution in the Neoproterozoic seas are characterized by high alkalinities, elevated Mg/Ca ratios (>7) and high supersaturations. Although direct precipitation of dolomite has been largely unsuccessful in laboratory at low temperatures (e.g., Gregg et al., 2015; Land, 1998; Rodriguez-Blanco et al., 2015), previous experiments also revealed that protodolomite (stoichiometric but disordered dolomite) crystallizes when the Mg/Ca ratio in solution is as high as 43 (Ohde and Kitano, 1978). Thus, the direct crystallization of norsethite from solutions with high Mg/Ba, high alkalinity, and sufficient CO_3^{2-} reiterates the significance of solution chemistry in controlling the crystallization of dolomite-analogues, thereby indicating that dolomite can directly form in limited physicochemical conditions.

553 # Acknowledgements

554

555 This work was partially supported by the National Natural Science Foundation of China
556 (Nos. 41772030 and 41572026), National Key R&D Program of China (No.
557 2018YFA0702700), the Key Research Program of the Institute of Geology & Geophysics,
558 CAS (No. IGGCAS-201901), and the Fundamental Research Funds for the Central
559 Universities.

560

References

Albéric, M., Bertinetti, L., Zou, Z.Y., Fratzl, P., Habraken, W., Politi, Y. (2018) The crystallization of amorphous calcium carbonate is kinetically governed by ion impurities and water. Advanced Science 5, 1701000.

Böttcher, M.E. (2000) Stable isotope fractionation during experimental formation of Norsethite ($BaMg[CO_3]_2$): A mineral analogue of dolomite. Aquatic Geochemistry 6, 201-212.

Böttcher, M.E., Effenberger, H.S., Gehlken, P.L., Grathoff, G.H., Schmidt, B.C., Geprägs, P., Bahlo, R., Dellwig, O., Leipe, T., Winde, V., Deutschmann, A., Stark, A., Gallego-Torres, D. and Martinez-Ruiz, F. (2012a) $BaMn[CO_3]_2$ – a previously unrecognized double carbonate in low-temperature environments: Structural, spectroscopic, and textural tools for future identification. Chemie der Erde - Geochemistry 72, 85-89.

Böttcher, M.E., Gehlken, P.L., Skogby, H. and Reutel, C. (1997) The vibrational spectra of $BaMg(CO_3)_2$ (norsethite). Mineralogical Magazine 61.

Böttcher, M.E., Geprags, P., Neubert, N., von Allmen, K., Pretet, C., Samankassou, E. and Nagler, T.F. (2012b) Barium isotope fractionation during experimental formation of the double carbonate $BaMn[CO_3]_2$ at ambient temperature. Isotopes Environ Health Stud 48, 457-463.

Bromiley, F.A., Ballaran, T.B., Langenhorst, F. and Seifert, F. (2007) Order and miscibility in the otavite-magnesite solid solution. American Mineralogist 92, 829-836.

Buzgar, N. and Apopei, A. I. (2009). The Raman study of certain carbonates. Geologie Tomul L, 2, 97-112.

Chai, L. and Navrotsky, A. (1996) Synthesis, characterization, and energetics of solid solution along the dolomite-ankerite join, and implications for the stability of ordered $CaFe(CO_3)_2$. American Mineralogist 81, 1141-1147.

Chang, L.L.Y. (1964) Synthesis of $MBa(CO_3)_2$ compounds. American Mineralogist 49, 1142.

Chukanov, N. V. (2014) The Application of IR Spectroscopy to the Investigation of Minerals.

590 Infrared spectra of mineral species. Springer Netherlands.

591 De Choudens-Sanchez, V. and Gonzalez, L.A. (2009) Calcite and Aragonite Precipitation
592 Under Controlled Instantaneous Supersaturation: Elucidating the Role of $CaCO_3$
593 Saturation State and Mg/Ca Ratio on Calcium Carbonate Polymorphism. Journal of
594 Sedimentary Research 79, 363-376.

595 Deelman, J. (2003) Low-temperature formation of dolomite and magnesite. Compact disc
596 publications Eindhoven.

597 Effenberger, H. and Zemann, J. (1985) Single crystal X-ray investigation of norsethite,
598 $BaMg(CO_3)_2$: one more mineral with an aplanar carbonate group. Zeitschrift für
599 Kristallographie 171, 275-280.

600 Ende, M., Effenberger, H. and Miletich, R. (2017) Evolution of the α-$BaMg(CO_3)_2$
601 low-temperature superstructure and the tricritical nature of its α–β phase transition.
602 Structural Science Crystal Engineering Materials. B73: 827-835.

603 Folk, R. L. and Land, L. S. (1975) Mg/Ca ratio and salinity: two controls over crystallization
604 of dolomite. AAPG bulletin, 59(1), 60-68.

605 Froese, E. (1967) A note on strontium magnesium carbonate. The Canadian Mineralogist 9,
606 65-70.

607 Frondel, C. and Bauer, L. (1955) Kutnahorite – a manganese dolomite, $CaMn(CO_3)_2$,
608 American Mineralogist. Mineralogical Soc Amer 1015 Eighteenth St, Nw Suite 601,
609 Washington, DC 20036, pp. 316-316.

610 Gaines, A.M. (1980) Dolomitization kinetics: recent experimental studies.

611 Given, R. K. and Wilkinson, B. H. (1985). Kinetic control of morphology, composition, and
612 mineralogy of abiotic sedimentary carbonates. Journal of Sedimentary Research, 55(1),
613 109-119.

614 Gregg, J.M., Bish, D.L., Kaczmarek, S.E., Machel, H.G. and Hollis, C. (2015) Mineralogy,
615 nucleation and growth of dolomite in the laboratory and sedimentary environment: A
616 review. Sedimentology 62, 1749-1769.

617 Hasiuk, F.J. and Lohmann, K.C. (2010) Application of calcite Mg partitioning functions to
618 the reconstruction of paleocean Mg/Ca. Geochimica et Cosmochimica Acta 74,
619 6751-6763.

620 Hood, A.v.S., Wallace, M.W. and Drysdale, R.N. (2011) Neoproterozoic aragonite-dolomite
621 seas? Widespread marine dolomite precipitation in Cryogenian reef complexes. Geology
622 39, 871-874.
623 Hood, A.v.S. and Wallace, M.W. (2012) Synsedimentary diagenesis in a Cryogenian reef
624 complex: Ubiquitous marine dolomite precipitation. Sedimentary Geology 255, 56-71.
625 Hood, W.C., Steidl, P.F., Tschopp, D.G. (1974) Precipitation of norsethite at room
626 temperature. American Mineralogist 59, 471-474.
627 Hubbard, C.R. and Snyder, R.L. (1988) RIR-measurement and use in quantitative XRD.
628 Powder Diffraction 3, 74-77.
629 Kaczmarek, S.E. and Sibley, D.F. (2007) A Comparison of Nanometer-Scale Growth and
630 Dissolution Features on Natural and Synthetic Dolomite Crystals: Implications for the
631 Origin of Dolomite. Journal of Sedimentary Research 77, 424-432.
632 Kaczmarek, S.E. and Sibley, D.F. (2011) On the evolution of dolomite stoichiometry and
633 cation order during high-temperature synthesis experiments: An alternative model for the
634 geochemical evolution of natural dolomites. Sedimentary Geology 240, 30-40.
635 Katz, A. and Matthews, A. (1977) The dolomitization of $CaCO_3$: an experimental study at
636 252–295 °C. Geochimica et Cosmochimica Acta 41, 297-308.
637 Kelleher, I.J. and Redfern, S.A.T. (2002) Hydrous calcium magnesium carbonate, a possible
638 precursor to the formation of sedimentary dolomite. Molecular Simulation 28, 557-572.
639 Land, L.S. (1967) Diagenesis of skeletal carbonates. Journal of Sedimentary Research 37.
640 Land, L.S. (1998) Failure to Precipitate Dolomite at 25 °C from Dilute Solution Despite
641 1000-Fold Oversaturation after 32 Years. Aquatic Geochemistry 4, 361-368.
642 Lindner, M. and Jordan, G. (2018) On the growth of witherite and its replacement by the
643 Mg-bearing double carbonate norsethite: Implications for the dolomite problem.
644 American Mineralogist 103, 252-259.
645 Lindner, M., Saldi, G.D., Carrocci, S., Bénézeth, P., Schott, J. and Jordan, G. (2018) On the
646 growth of anhydrous Mg-bearing carbonates – Implications from norsethite growth
647 kinetics. Geochimica et Cosmochimica Acta 238, 424-437.
648 Lindner, M., Saldi, G.D., Jordan, G. and Schott, J. (2017) On the effect of aqueous barium on

magnesite growth – A new route for the precipitation of the ordered anhydrous Mg-bearing double carbonate norsethite. Chemical Geology 460, 93-105.

Lindtke, J., Ziegenbalg, S. B., Brunner, B., Rouchy, J. M., Pierre, C., and Peckmann, J. (2011) Authigenesis of native sulphur and dolomite in a lacustrine evaporitic setting (Hellin basin, Late Miocene, SE Spain). Geological Magazine, 148(4), 655-669.

Lippmann, F. (1967) Die Kristallstruktur des Norsethit, $BaMg(CO_3)_2$, im Vergleich zum Dolomit, $CaMg(CO_3)_2$. Naturwissenschaften 54, 514-514.

Lippmann, F. (1968) Syntheses of $BaMg(CO_3)_2$ (Norsethite) at 20 °C and the Formation of Dolomite in Sediments. Recent developments in carbonate sedimentology in Central Europe. Springer, Berlin, Heidelberg, 33-37.

Lippmann, F. (1973) Sedimentary Caronate Minerals, Minerals, Rocks and Inorganic Materials. Monograph Series of Theoretical and Experimental Studies, Vol. 6. Spgigger-Verlag, Berlin 54.

Longo, J.M. and Voight, K.C. (1989) Synthesis of mixed-metal carbonates by grinding. Solid State Ionics 32, 409-412.

Loste, E., Wilson, R.M., Seshadri, R. and Meldrum, F.C. (2003) The role of magnesium in stabilising amorphous calcium carbonate and controlling calcite morphologies. Journal of Crystal Growth 254, 206-218.

Malone, M.J., Baker, P.A. and Burns, S.J. (1996) Recrystallization of dolomite: An experimental study from 50-200 °C. Geochimica et Cosmochimica Acta 60, 2189-2207.

Miser, D. E., Swinnea, J. S., and Steinfink, H. (1987). TEM observations and X-ray crystal-structure refinement of a twinned dolomite with a modulated microstructure. American Mineralogist, 72(1-2), 188-193.

Morrow, D.W. and Ricketts, B.D. (1986) Chemical controls on the precipitation of mineral analogues of dolomite: The sulfate enigma. Geology 14, 408-410.

Mrose, M.E.C., E.C.T.; Fahey, J. J.; Milton, C. (1961) Norsethite, $BaMg(CO_3)_2$, A new mineral from the Green River formation, Wyoming. American Mineralogisr 46, 420-429.

Ohde, S. and Kitano, Y. (1978) Synthesis of protodolomite from aqueous solution at normal temperature and pressure. Geochemical Journal 12, 115-119.

678 Peacor, D.R., Essene, E.J. and Gaines, A. (1987) Petrologic and crystal-chemical implications
679 of cation order-disorder in kutnahorite [$CaMn(CO_3)_2$]. American Mineralogist 72,
680 319-328.
681 Pimentel, C. and Pina, C.M. (2014) The formation of the dolomite-analogue norsethite:
682 Reaction pathway and cation ordering. Geochimica et Cosmochimica Acta 142, 217-223.
683 Pimentel, C. and Pina, C.M. (2016) Reaction pathways towards the formation of
684 dolomite-analogues at ambient conditions. Geochimica et Cosmochimica Acta 178,
685 259-267.
686 Platt, R.G. and Woolley, A.R. (1990) The carbonatites and fenites of Chipman Lake, Ontario.
687 Canadian Mineralogist 28, 241-250.
688 Politi, Y., Batchelor, D.R., Zaslansky, P., Chmelka, B.F., Weaver, J.C., Sagi, I., Weiner, S.
689 and Addadi, L. (2010) Role of Magnesium Ion in the Stabilization of Biogenic
690 Amorphous Calcium Carbonate: A Structure-Function Investigation. Chemistry of
691 Materials 22, 161-166.
692 Ries, J.B. (2009) Effects of secular variation in seawater Mg/Ca ratio (calcite-aragonite seas)
693 on $CaCO_3$ sediment production by the calcareous algae Halimeda, Penicillus and Udotea
694 – evidence from recent experiments and the geological record. Terra Nova 21, 323-339.
695 Ries, J.B., Anderson, M.A. and Hill, R.T. (2008) Seawater Mg/Ca controls polymorph
696 mineralogy of microbial $CaCO_3$: a potential proxy for calcite-aragonite seas in
697 Precambrian time. Geobiology 6, 106-119.
698 Rodriguez-Blanco, J.D., Shaw, S., Bots, P., Roncal-Herrero, T., Benning, L. G. (2012). The
699 role of pH and Mg on the stability and crystallization of amorphous calcium carbonate.
700 Journal of Alloys and Compounds, 536, S477-S479.
701 Rodriguez-Blanco, J.D., Shaw, S. and Benning, L.G. (2015) A route for the direct
702 crystallization of dolomite. American Mineralogist 100, 1172-1181.
703 Schmidt, B.C., Gehlken, P.L. and Böttcher, M.E. (2013) Vibrational spectra of $BaMn(CO_3)_2$
704 and a re-analysis of the Raman spectrum of $BaMg(CO_3)_2$. European Journal of
705 Mineralogy 25, 137-144.
706 Segev, E. and Erez, J. (2006) Effect of Mg/Ca ratio in seawater on shell composition in
707 shallow benthic foraminifera. Geochemistry, Geophysics, Geosystems 7(2).

Sibley, D.F. (1990) Unstable to stable transformations during dolomitization. The Journal of Geology 98, 739-748.

Sibley, D.F., Nordeng, S.H. and Borkowski, M.L. (1994) Dolomitization kinetics of hydrothermal bombs and natural settings. Journal of Sedimentary Research 64, 630-637.

Steyn, J. and Watson, M. (1967) Notes on a new occurrence of norsethite $BaMg(CO_3)_2$. American Mineralogist 52, 1770-1775.

Tareen, J., Fazeli, A., Basavalingu, B. and Bhandige, G. (1995) Decarbonation curves and associated thermodynamic data for synthetic Cd-dolomites $CdMg(CO_3)_2$, $CdMn(CO_3)_2$ and $CdZn(CO_3)_2$. Journal of Thermal Analysis and Calorimetry 44, 937-954.

Wang, D., Wallace, A.F., De Yoreo, J.J. and Dove, P.M. (2009) Carboxylated molecules regulate magnesium content of amorphous calcium carbonates during calcification. Proc Natl Acad Sci USA 106, 21511-21516.

Wang, X., Ye, Y., Wu, X., Smyth, J. R., Yang, Y., Zhang, Z. and Wang, Z. (2019). High-temperature Raman and FTIR study of aragonite-group carbonates. Physics and Chemistry of Minerals, 46(1), 51-62.

Wang, Y. Y., Yao, Q. Z., Zhou, G. T., Fu, S. Q. (2015) Transformation of amorphous calcium carbonate into monohydrocalcite in aqueous solution: a biomimetic mineralization study. European Journal of Mineralogy, 27(6), 717-729.

Warren, J. (2000) Dolomite occurrence, evolution and economically important associations. Earth-Science Reviews 52, 1-81.

Xu, J., Yan, C., Zhang, F., Konishi, H., Xu, H. and Teng, H.H. (2013) Testing the cation-hydration effect on the crystallization of Ca-Mg-CO_3 systems. Proc Natl Acad Sci USA 110, 17750-17755.

Zheng, Y.F. and Böttcher, M.E. (2016) Oxygen isotope fractionation in double carbonates. Isotopes Environ Health Stud 52, 29-46.

Zhou, G.T., Guan, Y.B., Yao, Q.Z. and Fu, S.Q. (2010) Biomimetic mineralization of prismatic calcite mesocrystals: Relevance to biomineralization. Chemical Geology 279, 63-72.

This is the peer-reviewed, final accepted version for American Mineralogist, published by the Mineralogical Society of America.
The published version is subject to change. Cite as Authors (Year) Title. American Mineralogist, in press.
DOI: https://doi.org/10.2138/am-2021-7348. http://www.minsocam.org/

Table 1. Experimental parameters in the mineralization of norsethite, and the minimum carbonate concentration required for oversaturation with respect to witherite and norsethite.

$[Mg^{2+}]_0$ (mM)	$[Ba^{2+}]_0$ (mM)	Mg/Ba ratio	$pH_{initial}$	The minimum $[CO_3^{2-}]$ required for specific mineral oversaturation ($\times 10^{-3}$ mM)		Mineralization Duration (hour)
				witherite	norsethite	
50	25	2	6.3	0.110	0.039	0.5, 1, 2, 6, 12, 24, 48
50	10	5	5.5	0.275	0.061	0.5, 1, 2, 6, 12, 24, 48
50	5	10	5.6	0.551	0.086	0.5, 1, 2, 6, 12, 24, 48

This is the peer-reviewed, final accepted version for American Mineralogist, published by the Mineralogical Society of America.
The published version is subject to change. Cite as Authors (Year) Title. American Mineralogist, in press.
DOI: https://doi.org/10.2138/am-2021-7348. http://www.minsocam.org/

754

755

756

757

758 Table 2. Time for first detection of norsethite (t_{nor}) and solution chemistry at t_{nor}.

759

760

Mg/Ba ratio (mM/mM)	Time for first detection of norsethite (t_{nor}; hours)	$pH_{t,nor}$	$[Ba^{2+}]_{t, nor}$ (mM)	$[Mg^{2+}]_{t, nor}$ (mM)	$Mg/Ba_{t, nor}$	$[CO_3^{2-}]_{t, nor}$ (mM) measured by titration
50/25	12	8.48	2.17	45.23	20.84	12.85
50/10	6	8.78	1.30	47.59	36.61	18.15
50/5	2	8.60	1.88	49.10	26.12	3.54

761

762

763

764

765

766

767

This is the peer-reviewed, final accepted version for American Mineralogist, published by the Mineralogical Society of America.
The published version is subject to change. Cite as Authors (Year) Title. American Mineralogist, in press.
DOI: https://doi.org/10.2138/am-2021-7348. http://www.minsocam.org/

768

769 Table 3. Experimental parameters and the minimum carbonate concentration required for oversaturation with respect to witherite and norsethite.

$[Mg^{2+}]_0$ (mM)	$[Ba^{2+}]_0$ (mM)	Mg/Ba ratio	$pH_{initial}$	The minimum $[CO_3^{2-}]^-$ required for specific mineral oversaturation ($\times 10^{-3}$ mM)		Mineralization Duration (hour)
				witherite	norsethite	
50	2	25	5.5	1.377	0.136	1, 2, 3, 4, 6, 12, 24, 48
25	1	25	5.3	2.754	0.273	1, 2, 3, 4, 6, 12, 24, 48
100	4	25	5.4	0.689	0.068	1, 2, 3, 4, 6, 12, 24, 48
200	8	25	5.6	0.344	0.034	1, 2, 3, 4, 6, 12, 24, 48
400	16	25	5.5	0.172	0.017	1, 2, 3, 4, 6, 12, 24, 48
80	2	40	5.4	1.377	0.108	4
40	2	20	5.5	1.377	0.153	4
30	2	15	5.4	1.377	0.176	4
20	2	10	5.5	1.377	0.216	4
10	2	5	5.6	1.377	0.305	4
2	2	1	5.8	1.377	0.682	4

770

Figure captions

Figure 1. Electron micrographs of the precipitates after 40 min (a1), 1 (a2) and 2 h (a3) of mineralization at initial Mg/Ba of 50/25, and the micro-Raman spectrum of the precipitate in panel a1 (Inset on panel a1). Electron micrographs of the precipitates after 1 (b1) and 2 h (b3) of mineralization at initial Mg/Ba of 50/10, and micro-Raman spectrum (b2) of the precipitate in panel b1. Electron micrographs of the precipitates after 1 (c1) and 2 h (c2) of mineralization at initial Mg/Ba of 50/5, and the EDS spectra (c3 and c4) of the different particles in panel c2.

Figure 2. Powder X-ray patterns of the products after 2 h of mineralization in the experiments with Mg/Ba of 50/25 (a), 50/10 (b), and 50/5 (c).

Figure 3. Typical powder XRD patterns of the products at t_{nor} in the experiments with Mg/Ba of 50/25 and 50/10.

Figure 4. Electron micrographs of the products at t_{nor} in the experiments with Mg/Ba of 50/25 (a) and 50/10 (b), and the magnified images of the products at Mg/Ba of 50/10 after 12 (c), 24 (d) and 48 h (e) of mineralization.

Figure 5. Plot of percent norsethite vs. time at Mg/Ba of 50/25, 50/10 and 50/5.

Figure 6. Time-dependent evolution of $[Ba^{2+}]$, $[Mg^{2+}]$ and pH in solution in the experiments with initial Mg/Ba of 50/25 (a), 50/10 (b), and 50/5 (c) during mineralization. The cross mark denotes the solution chemical parameters, i.e., ion concentrations and pH at t_{nor}.

Figure 7. Electron micrographs of the products at Mg/Ba of 50/2 after 2 (a) and 3 h (b), corresponding Raman spectra (c), and representative EDX spectrum of the precipitate particles inserted in Panel a. Powder XRD pattern (d), and FT-IR spectrum (e) and Electron micrographs (f) of the product after 4 h of mineralization. Electron micrographs of the products after 8 (g), 12 (h), and 36 h (i) of mineralization.

Figure 8. Time-dependent evolution of $[Ba^{2+}]$, $[Mg^{2+}]$, pH in solution in the experiments with an initial Mg/Ba ratio of 50/2.

799 Figure 9. Electron micrographs of typical mineralized products at Mg/Ba of 25/1 (a), 200/8 (b)
800 and 400/16 (c) after 4 h of mineralization.
801 Figure 10. Powder XRD patterns (a) and the magnified spectra between 22-26^{o} 2θ (b) of the
802 products in experiments with Mg/Ba of 2/2, 10/2, 20/2, 30/2, 40/2 and 80/2 after 4 h
803 of mineralization. N: the characteristic diffraction of norsethite; W: the
804 characteristic diffraction of witherite.
805 Figure 11. Electron micrographs of typical products at Mg/Ba of 20/2 (a), 30/2 (b), 40/2 (c),
806 and 80/2 (d) after 4 h of mineralization.
807

This is the peer-reviewed, final accepted version for American Mineralogist, published by the Mineralogical Society of America.
The published version is subject to change. Cite as Authors (Year) Title. American Mineralogist, in press.
DOI: https://doi.org/10.2138/am-2021-7348. http://www.minsocam.org/

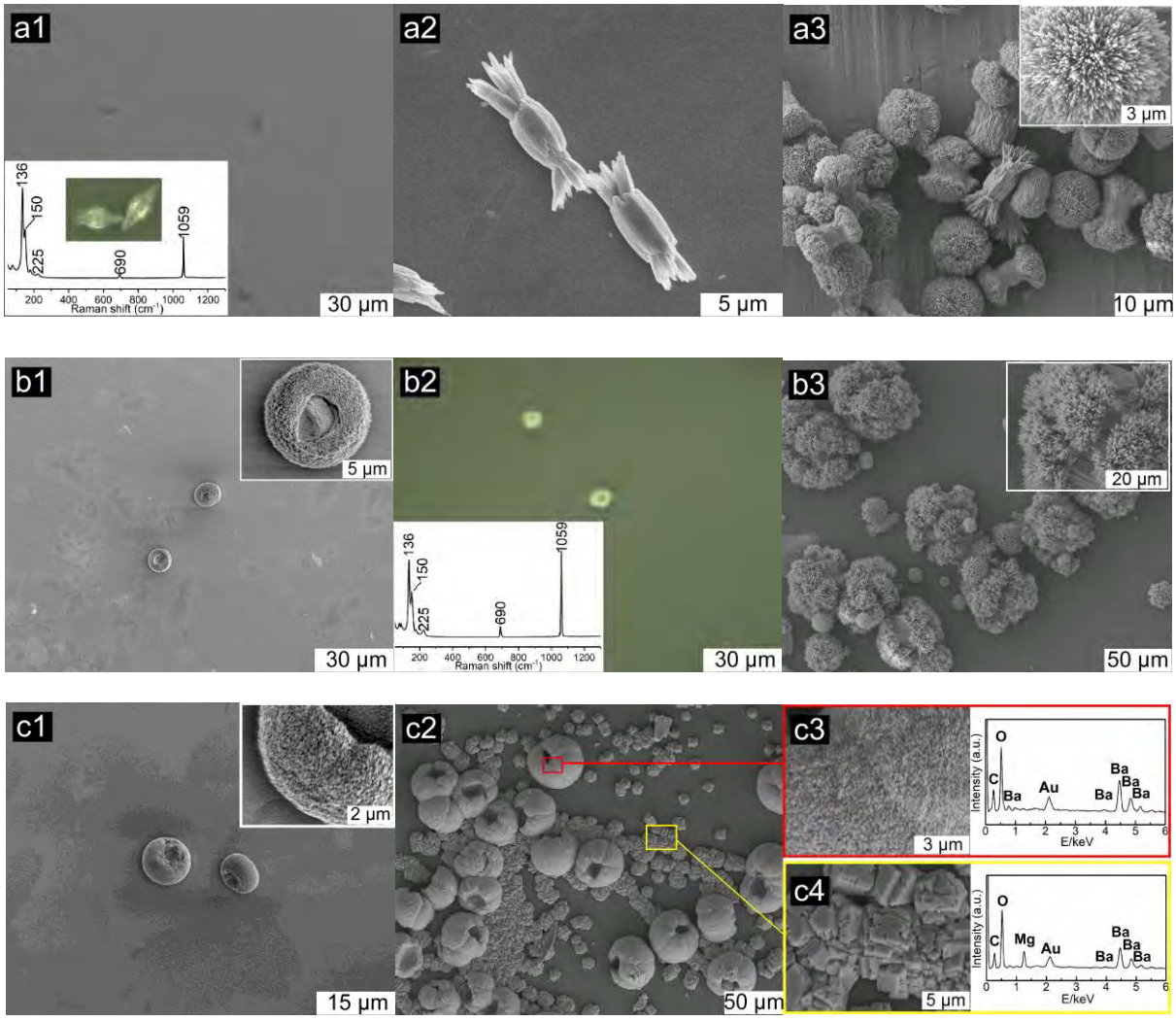

Figure 1

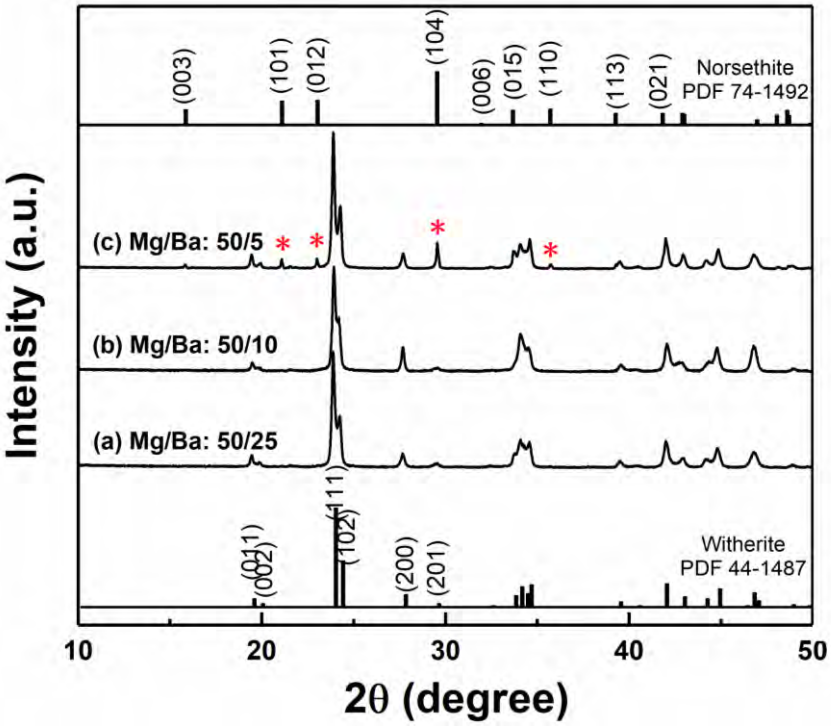

Figure 2

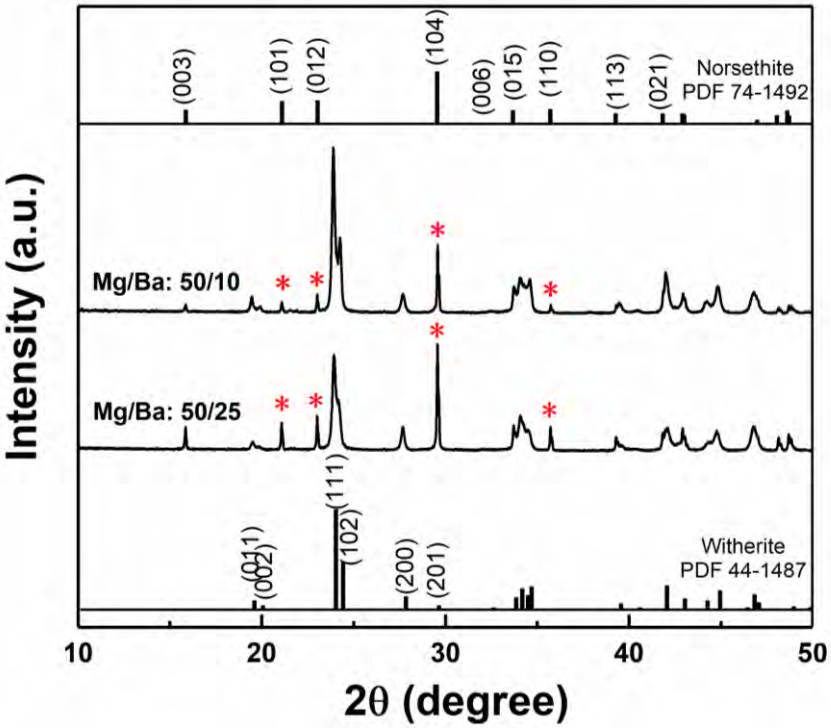

Figure 3

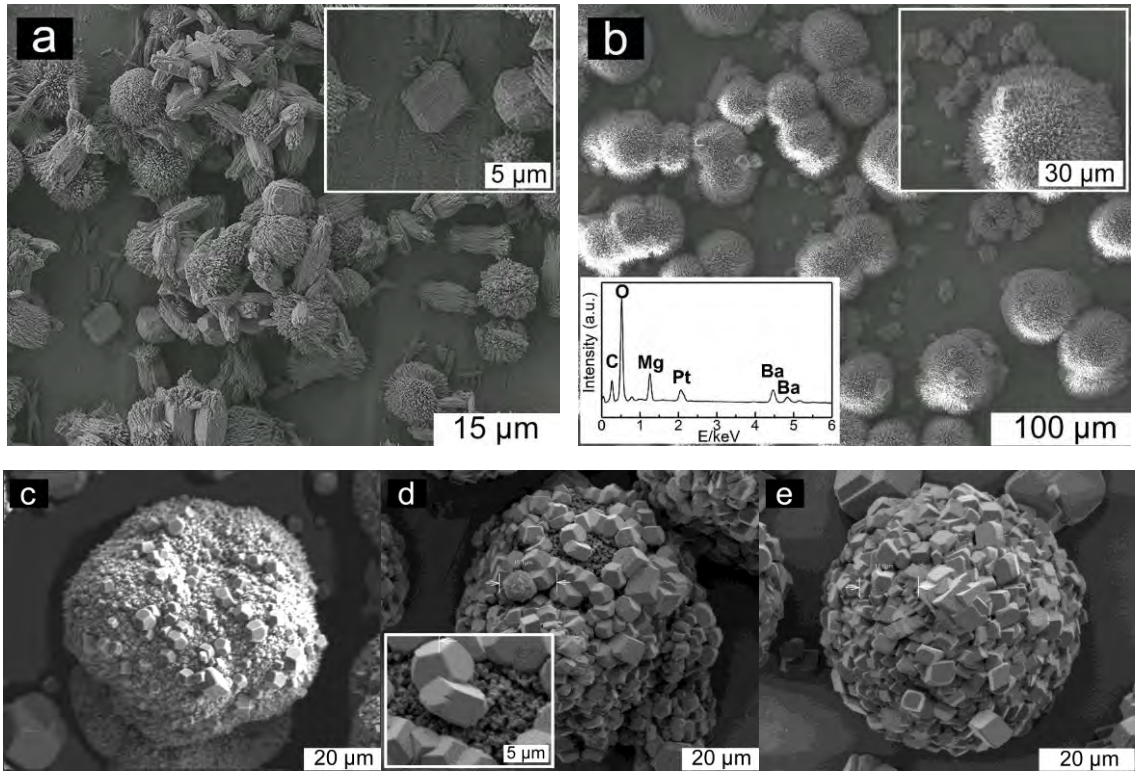

Figure 4

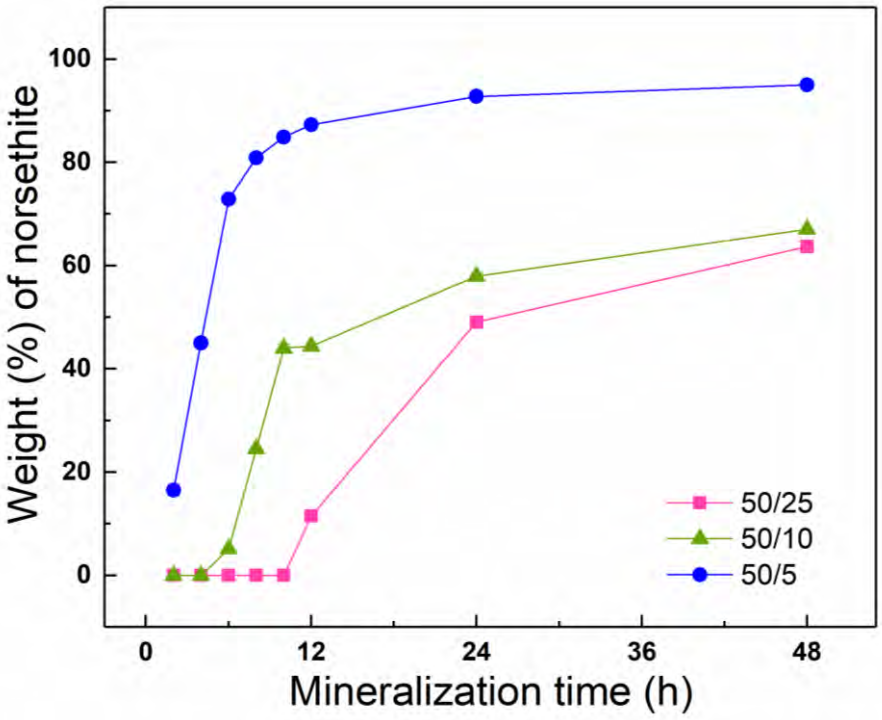

Figure 5

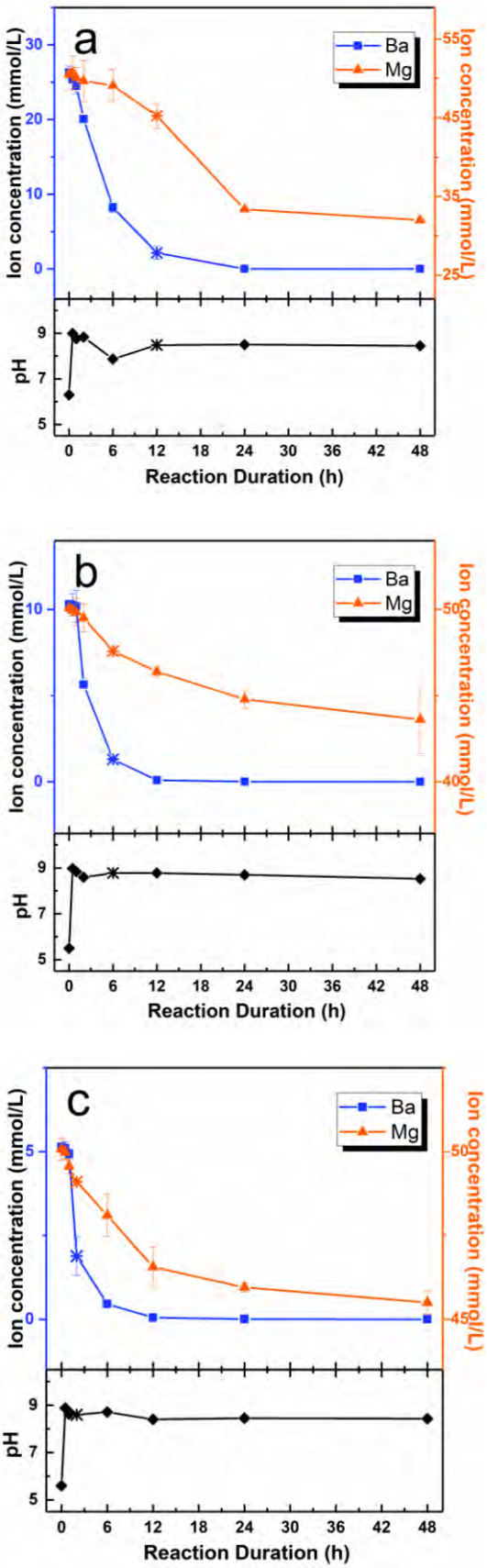

Figure 6

This is the peer-reviewed, final accepted version for American Mineralogist, published by the Mineralogical Society of America.
The published version is subject to change. Cite as Authors (Year) Title. American Mineralogist, in press.
DOI: https://doi.org/10.2138/am-2021-7348. http://www.minsocam.org/

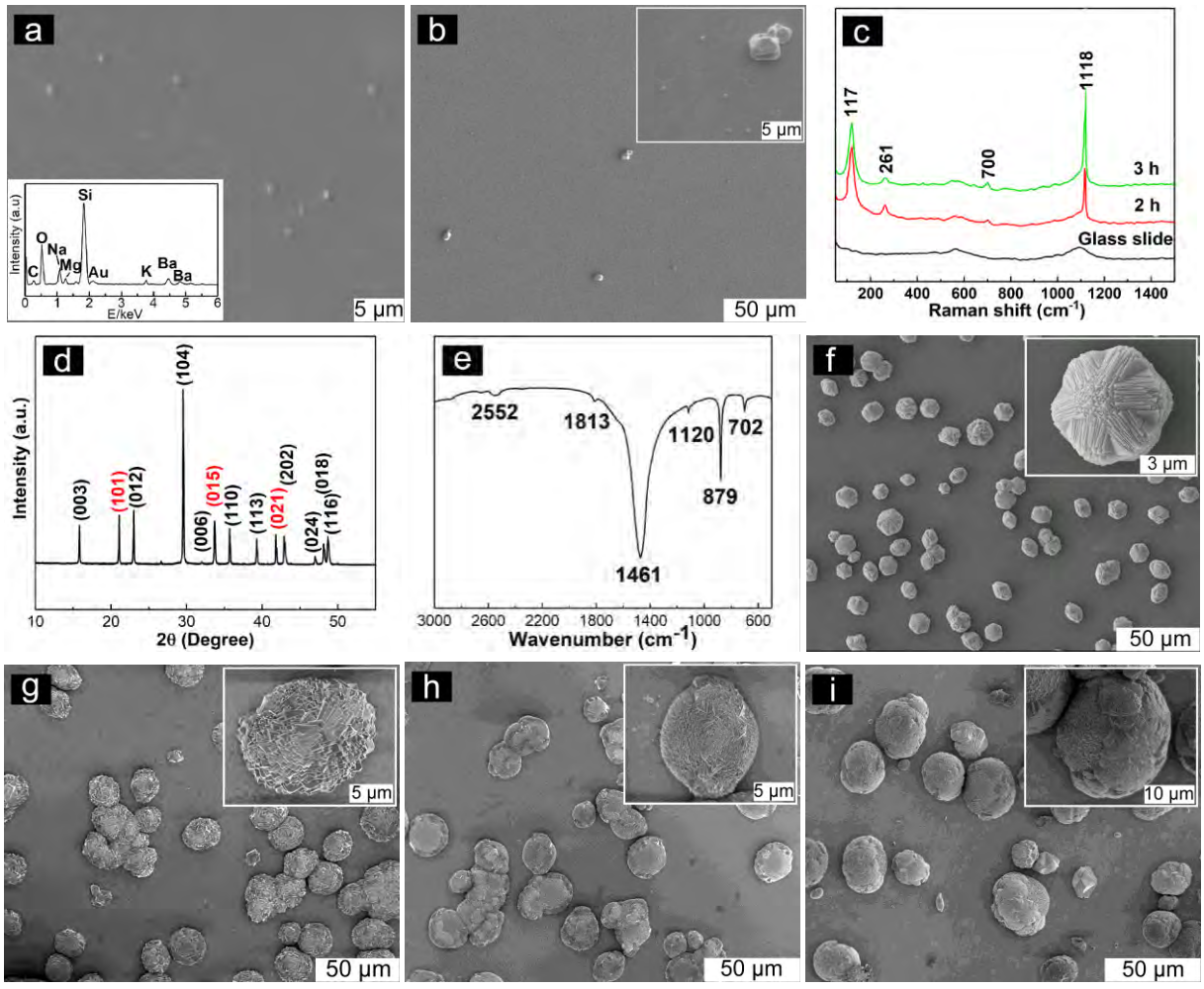

Figure 7

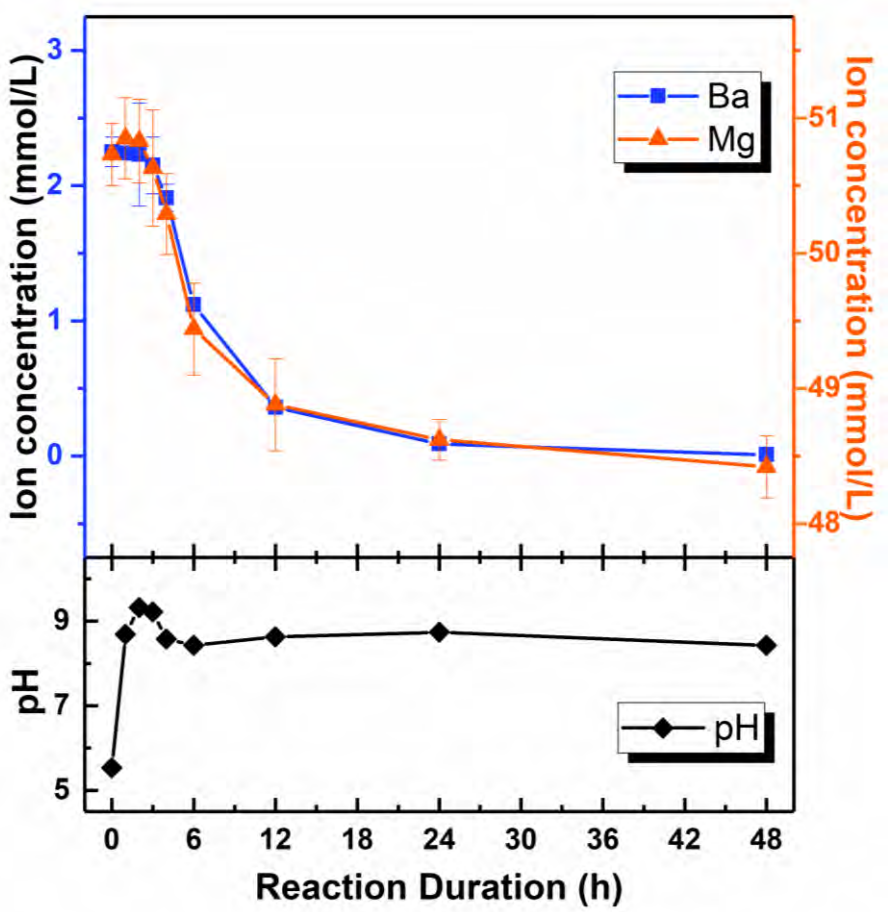

Figure 8

This is the peer-reviewed, final accepted version for American Mineralogist, published by the Mineralogical Society of America.
The published version is subject to change. Cite as Authors (Year) Title. American Mineralogist, in press.
DOI: https://doi.org/10.2138/am-2021-7348. http://www.minsocam.org/

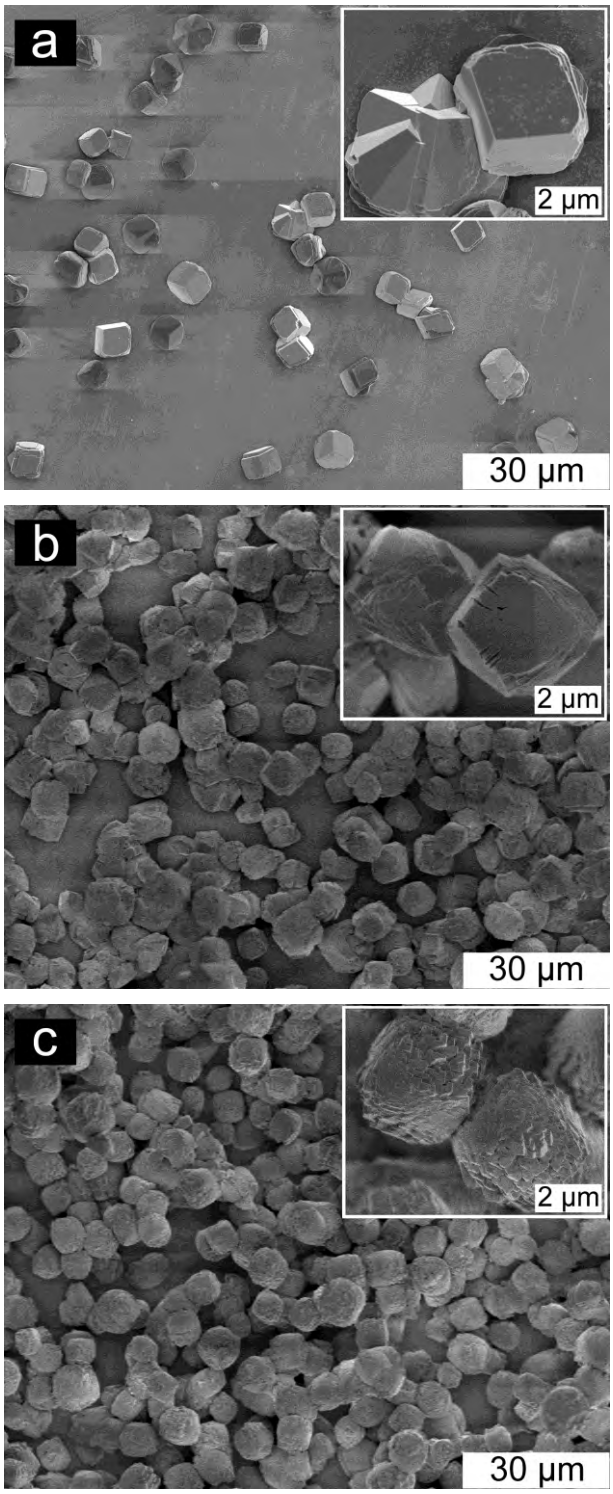

Figure 9

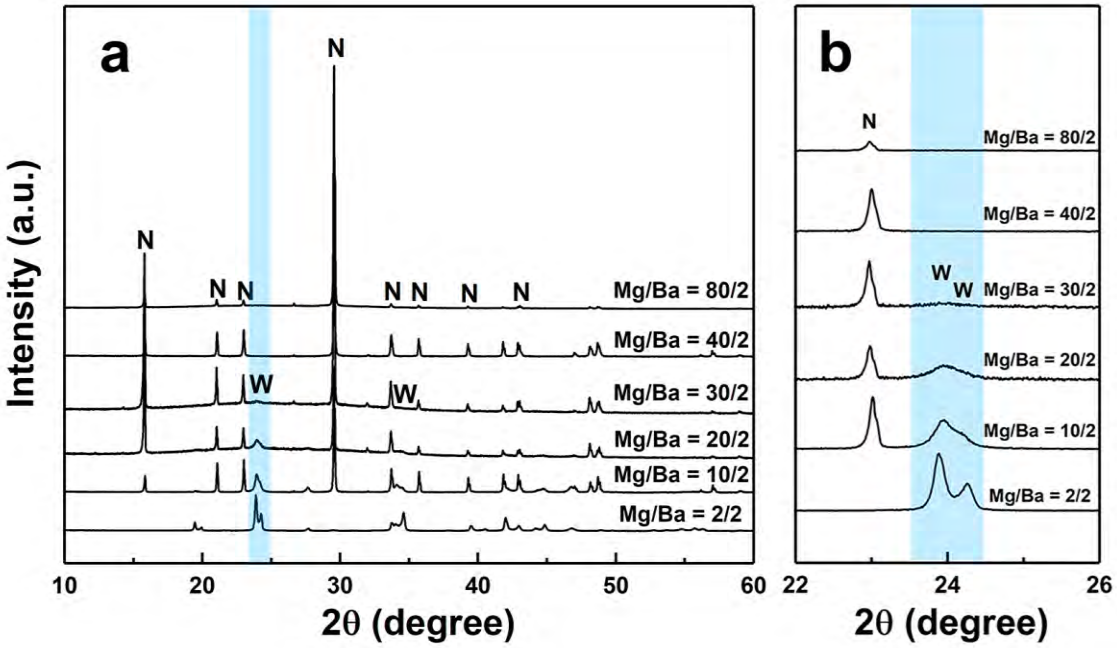

Figure 10

This is the peer-reviewed, final accepted version for American Mineralogist, published by the Mineralogical Society of America.
The published version is subject to change. Cite as Authors (Year) Title. American Mineralogist, in press.
DOI: https://doi.org/10.2138/am-2021-7348. http://www.minsocam.org/

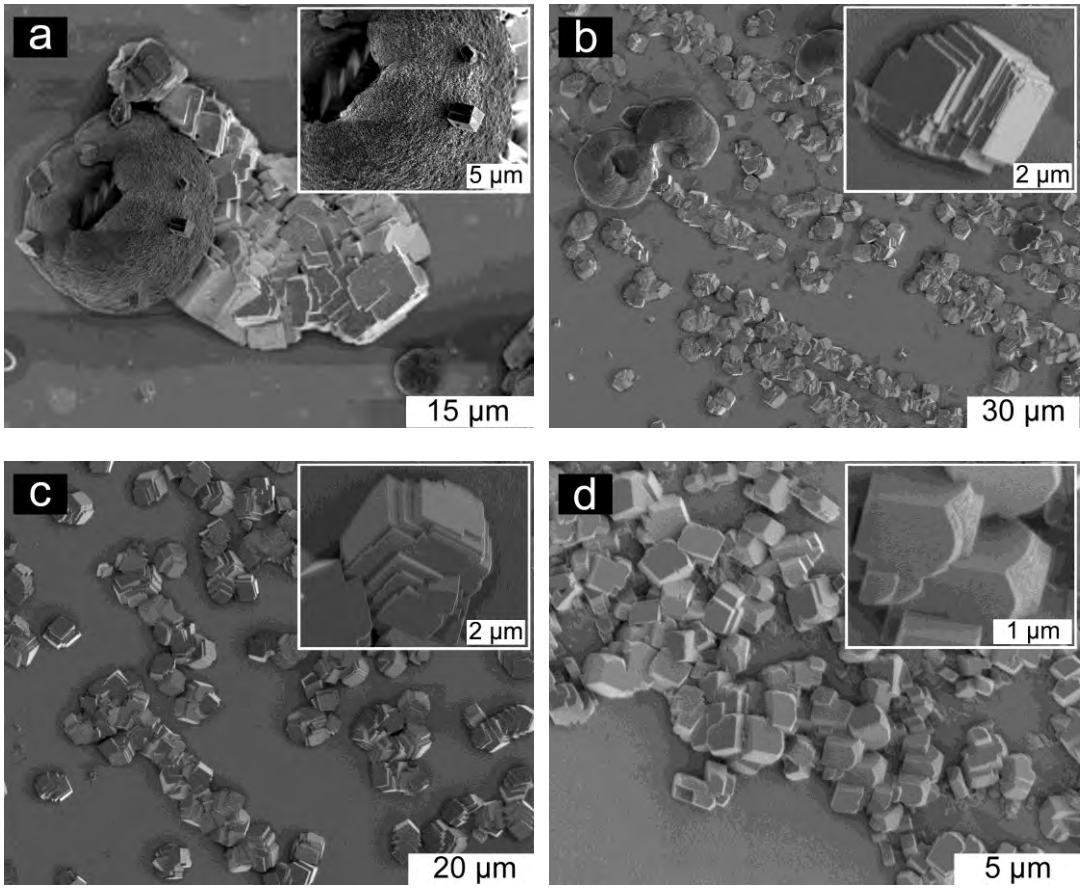

Figure 11